



1 **Elevated CO₂, increased leaf-level productivity and water-use efficiency during the early Miocene**

2

3 Tammo Reichgelt^{1,2}, William J. D'Andrea¹, Ailín del C. Valdivia-McCarthy¹, Bethany R.S. Fox³, Jennifer
4 M. Bannister⁴, John G. Conran⁵, William G. Lee^{6,7}, Daphne E. Lee⁸

5

6 ¹Lamont-Doherty Earth Observatory, Columbia University, Palisades, New York, USA.

7 ²Department of Geosciences, University of Connecticut, Storrs, Connecticut, USA.

8 ³Department of Biological and Geographical Sciences, University of Huddersfield, Huddersfield, UK.

9 ⁴Department of Botany, University of Otago, Dunedin, New Zealand.

10 ⁵ACEBB & SGC, School of Biological Sciences, The University of Adelaide, Adelaide, Australia.

11 ⁶Landcare Research, Dunedin, New Zealand.

12 ⁷School of Biological Sciences, University of Auckland, Auckland, New Zealand.

13 ⁸Department of Geology, University of Otago, Dunedin, New Zealand.

14 Correspondence: Tammo Reichgelt (tammo.reichgelt@uconn.edu)

15

16 **Abstract.** Rising atmospheric CO₂ is expected to increase global temperatures, plant water-use efficiency,
17 and carbon storage in the terrestrial biosphere. A CO₂ fertilization effect on terrestrial vegetation is
18 predicted to cause global greening as the potential ecospace for forests expands. However, leaf-level
19 fertilization effects, such as increased productivity and water-use efficiency, have not been documented
20 from fossil leaves in periods of heightened atmospheric CO₂. Leaf gas-exchange rates reconstructed from
21 early Miocene fossils which grew at southern temperate and tropical latitudes, when global average
22 temperatures were 5–6°C higher than today reveal that atmospheric CO₂ was ~450–550 ppm. Early
23 Miocene CO₂ is similar to projected values for 2040AD, and consistent with Earth System Sensitivity of
24 3–7°C to a doubling of CO₂. While early Miocene leaves had photosynthetic rates similar to modern
25 plants, southern temperate leaves were more productive than modern due to a longer growing season.
26 This higher productivity was likely mirrored at northern temperate latitudes as well, where a greater



27 availability of landmass would have led to increased carbon storage in forest biomass relative to today.
28 Intrinsic water-use efficiency of both temperate and tropical forest trees was high, toward the upper limit
29 of the range for modern trees, which likely expanded the habitable range in regions that could not support
30 forests with high moisture demands under lower atmospheric CO₂. Overall, early Miocene elevated
31 atmospheric CO₂ sustained globally higher temperatures and our results reveal the first empirical
32 evidence of concomitant enhanced intrinsic water-use efficiency, indicating a forest fertilization effect.

33

34 **1 Introduction**

35 Terrestrial plants comprise 450 Gt of carbon, representing 80% of Earth's dry carbon (C) biomass (Bar-on
36 et al., 2018). Globally, plants draw down ~120 Gt of atmospheric C per year through photosynthesis,
37 representing the largest annual C flux on Earth (Beer et al., 2010). Total plant biomass is believed to be
38 determined in large part by atmospheric carbon dioxide concentrations (C_a), and it is predicted that future
39 increases in C_a will have a three-pronged effect on the terrestrial biosphere: 1) increased global
40 temperatures will shift the boundaries of climate zones and thereby the potential forest expanse (Rubel
41 and Kottek, 2010); 2) productivity will increase because global photosynthesis is C limited and increased
42 C_a will make more C available to the terrestrial biosphere (Zhu et al., 2016); and 3) elevated C_a will
43 increase plant water-use efficiency and reduce the threshold for physiological drought (Cernusak, 2020),
44 making more land area available for biosphere expansion (Zhou et al., 2017). Plant fossils record the
45 effect of past changes in climate, including CO₂ enrichment, and thus fossil floras provide insight into
46 changes in the carbon cycle and their effects on the terrestrial biosphere from a natural, whole-ecosystem
47 perspective.

48 The Miocene has been considered problematic for our understanding of Earth System Sensitivity
49 (ESS) to C_a, because most proxy-based C_a estimates indicate concentrations near 300 ppm (Foster et al.,
50 2017), close to pre-industrial values, yet global temperatures were 5–6 °C higher than modern (Hansen et
51 al., 2013). Enhanced radiative forcing is required to maintain such elevated early Miocene temperatures
52 (Herold et al., 2010; Hansen et al., 2013), and without elevated C_a, climate models cannot achieve such



53 high global temperatures in the Miocene (Henrot et al., 2010). The early Miocene also had an expanded
54 biosphere compared to today, including woody vegetation in locations that are currently too cold and/or
55 too dry for forests (e.g. Askin and Raine, 2000; Herold et al., 2010). A biosphere of the magnitude
56 observed in the early Miocene fossil record requires elevated temperatures and plant water-use efficiency,
57 suggesting C_a levels higher than estimated by most existing proxy reconstructions (Herold et al., 2010;
58 Henrot et al., 2010). Importantly, plant-based C_a reconstructions have challenged the consensus of low C_a
59 in the early Miocene (Kürschner and Kvaček, 2009; Reichgelt et al., 2016; Tesfamichael et al., 2017;
60 Londoño et al., 2018) and previous interpretations of alkenone-based C_a proxies are being disputed
61 (Bolton et al., 2016; Witkowski et al., 2019).

62 We applied plant gas-exchange modeling (Franks et al., 2014) to fossil leaves from the early Miocene
63 (~23 Ma) rainforest ecosystem from southern New Zealand preserved in the Foulden Maar deposit
64 (Bannister et al., 2012; Reichgelt et al., 2013; Conran et al., 2014; Lee et al., 2016) to reconstruct carbon
65 assimilation rates (A_n), intrinsic water-use efficiency (iWUE; the ratio between carbon assimilation and
66 stomatal conductance to water), and the C_a levels required to maintain these values. The same analyses
67 were performed on previously published leaf $\delta^{13}C$ and micromorphological measurements from two early
68 Miocene fossil floras from Ethiopia (Tesfamichael et al., 2017) and Panama (Londoño et al., 2018).
69 Because A_n , iWUE, and C_a are interdependent (Farquhar et al., 1980; Drake et al., 1997), we
70 reconstructed these variables in concert for each fossilized leaf recovered from these forest ecosystems.
71 This allows us to make inferences concerning carbon availability, productivity, and water balance in the
72 forest.

73

74 **2 Methods**

75 **2.1 Site Description**

76 Foulden Maar (Fig. 1a) is a unique *Konservat-Lagerstätte* with abundantly preserved plants and insects
77 (Kaulfuss et al., 2015; Lee et al., 2016) in southern New Zealand (45.527°S, 170.219°E). It was formed in
78 an ancient maar-diatreme lake (Fig. 1b) at the Oligocene/Miocene boundary (Fox et al., 2015; Kaulfuss,



79 2017) and consists of ~100 kyr of annually laminated diatomite (Lindqvist and Lee, 2009; Fox et al.,
80 2016). The Foulden maar-diatreme complex is part of the larger late Oligocene – late Miocene Waipiata
81 Volcanic Field that produced a variety of maar volcanoes and scoria cones (Németh and White, 2003).
82 Plant fossils used in this study were collected from a ~183 m long drill core (Fig. 1c). The Lauraceae-
83 dominated rainforest (Bannister et al., 2012) surrounding the lake grew at ~50°S (Fig. 1a). The climate
84 was marginally subtropical with a mean annual temperature of ~18°C, similar to modern day climates at
85 30°S (Reichgelt et al., 2019). The length of the growing season in this climate was ~10 months, compared
86 to 5–6 months today, as reconstructed from the surface exposure macrofossil assemblage using the
87 Climate Leaf Analysis Multivariate Program (Reichgelt et al., 2013).

88

89 **2.2 Fossil leaf anatomy and paleoecology**

90 Mummified fossil leaves were extracted from turbidite deposits that occur frequently within the Foulden
91 Maar diatomite core (Fox et al., 2015). The diatomite is loosely consolidated allowing mummified leaves
92 to be extracted using a combination of water and scalpels. After extraction, the leaves were cut into three
93 pieces: one for bulk $\delta^{13}\text{C}$ analysis, one for stomatal conductance measurements, and a third as a reference
94 specimen. Leaf $\delta^{13}\text{C}$ was measured using a Costech elemental combustion system (EA) coupled to a Delta
95 V Plus IRMS (Thermo). In order to place measured $\delta^{13}\text{C}$ on the VPDB scale, we calibrated measurements
96 using a two-point isotope calibration based on the USGS40 and USGS41 standards. Measurement
97 uncertainty was calculated by replicating ~15 samples, and applying averaged uncertainty to the
98 remaining leaves. For conductance measurements the leaves were soaked in hydrogen peroxide (H_2O_2)
99 with up to 40% dilution, with tetra-sodium pyrophosphate salt crystals ($\text{Na}_4\text{P}_2\text{O}_7 \cdot 10[\text{H}_2\text{O}]$), on a boiling
100 plate at 40–50 °C for 1–2 hours (Bannister et al., 2012). When the adaxial and abaxial cuticle layer could
101 be separated, the leaf layers were cleaned of mesophyll cell debris using small paintbrushes and both
102 layers were stained with <0.5% Crystal Violet ($\text{C}_{25}\text{N}_3\text{H}_{30}\text{Cl}$) and mounted on glass slides with glycerin
103 jelly. Conductance measurements were made on 5–8 pictures at 100× magnification using TView
104 7.1.1.2 microscope imaging software on a Nikon Optiphot. Each picture was given bounding boxes ($0.3 \times$



105 0.3 mm) on which cells were counted, to calculate stomatal density, and stomatal size measurements were
106 made using ImageJ 1.48v software (Schneider et al., 2012).

107 18 distinct leaf morphotypes were identified from the Foulden Maar drill core. Descriptions and
108 justification for identification are found in the Supplementary Information. Species identifications are
109 provided, where possible, based on paleobotanical studies from the Foulden Maar surface exposures.
110 Known species recovered from the Foulden Maar drill core are *Litsea calicarioides* (Fig. S1a),
111 *Cryptocarya taieriensis* (Fig. S1b), *C. maarensis* (Fig. S1i), *Beilschmiedia otagoensis* (Fig. S2a)
112 (Lauraceae) (Bannister et al., 2012), *Laurelia otagoensis* (Fig. S2h) (Atherospermataceae) (Conran et al.,
113 2013), and *Hedycarya pluvisilva* (Fig. S2i) (Monimiaceae) (Conran et al., 2016). Otherwise, tentative
114 genus or family identifications are provided, or unspecified morphotypic qualifiers, for leaves that could
115 not be assigned a plant group. These will be henceforth be referred to as “C” (Fig. S1c), cf. Myrtaceae
116 (Fig. S1d), cf. *Ripogonum* (Fig. S1e), cf. *Myrsine* (Fig. S1f), “H” (Fig. S1g), cf.
117 Elaeocarpaceae/Cunoniaceae (Fig. S1h), cf. *Dysoxylum* (Fig. S2b), cf. *Cryptocarya* (Fig. S2c), “O” (Fig.
118 S2d), “P” (Fig. S2e), “Q” (Fig. S2f) and cf. *Endiandra* (Fig. S2g).

119 We made 375 anatomical and 80 carbon isotope measurements on 72 organically preserved fossil
120 leaves representing the 18 species collected from the Foulden Maar deposit (Fig. 1a). The affinities of
121 modern living relatives of the plant types at Foulden Maar strongly suggest that during the Miocene the
122 site was characterized by a multi-layered closed canopy rainforest ecosystem (Reichgelt et al., 2013;
123 Conran et al., 2014). In order to determine atmospheric carbon (C_a), intrinsic water-use efficiency
124 (iWUE), and carbon assimilation rates (A_n), the ecological strategies of the individual fossil species at
125 Foulden Maar need to first be established (Reichgelt and D’Andrea, 2019). Understory species rarely
126 experience light saturation and utilize respired CO_2 that has already undergone isotopic fractionation;
127 both conditions influence gas-exchange modelling results (Royer et al., 2019). Therefore, C_a
128 reconstructed from understory species cannot be considered indicative of true global C_a . Here, we
129 determine whether a fossil leaf type was likely in the canopy or the understory, based on 1) leaf $\delta^{13}C$, 2)
130 leaf cell density, and 3) sinuosity of the epidermal cell walls. A large range of leaf $\delta^{13}C$ in a single species



131 is indicative of different levels of light saturation, which indicates that this species may preferentially
132 occur in the subcanopy or in the understory (Graham et al., 2014). Leaves in the canopy, experiencing
133 light saturation, divide epidermal cells rapidly compared to leaves in the shade, leading to high cell
134 densities and relatively high leaf mass per areas in sun-exposed leaves (Šantrůček et al., 2014). Finally, a
135 high level of anticlinal cell wall sinuosity has been interpreted as indicative of low-light conditions
136 (Kürschner, 1997; Bush et al., 2017). We consider these three lines of evidence occurring in concert as
137 indicative of a canopy or subcanopy ecological preference.

138

139 **2.3 Modelling gas-exchange**

140 Atmospheric carbon dioxide (C_a), plant photosynthesis (A_n), and intrinsic water-use efficiency (iWUE)
141 are tightly linked (Farquhar et al., 1980; Drake et al., 1997), which allows us to solve for these parameters
142 iteratively, through anatomical and carbon isotope ($\delta^{13}\text{C}$) measurements of the fossil leaves. The Franks et
143 al. (2014) gas-exchange model solves for C_a , by iteratively reconstructing A_n and leaf conductance to
144 atmospheric carbon (G_c), using a Monte Carlo approach. This means that every C_a reconstruction has an
145 associated A_n and G_c value.

146

147

$$C_a = \frac{A_n}{G_c} \times \left(1 - \frac{C_i}{C_a}\right) \quad (1)$$

148

149 In which C_i/C_a represents the ratio of intercellular carbon to atmospheric carbon, which can be
150 reconstructed using known leaf fractionation processes: fractionation caused by diffusion (a),
151 carboxylation (b), and fractionation caused by the preferential uptake of ^{12}C to ^{13}C in photosynthesis (Δ),
152 which is also influenced by the rate at which the leaf is photosynthesizing (Farquhar et al., 1982).

153

154

$$\frac{C_i}{C_a} = \frac{\Delta - a}{b - a} \quad (2)$$



155

156 Here, $a = 4.4\text{‰}$ and $b = 29\text{‰}$ (Farquhar et al., 1982; Roeske and O'Leary, 1984). Δ can be calculated
157 from the $\delta^{13}\text{C}$ of the air, derived from Tipple et al. (2010) and measurements of leaf $\delta^{13}\text{C}$ (Farquhar and
158 Richards, 1984; Farquhar et al., 1989). Leaf and air $\delta^{13}\text{C}$ used in the Franks et al. (2014) model are
159 presented in Table S1.

160

161

$$\Delta = \frac{\delta^{13}C_{air} - \delta^{13}C_{leaf}}{1 + \delta^{13}C_{leaf}} \quad (3)$$

162

163 G_c is determined by the maximum capacity for conductance of a leaf surface (G_{max}), the ratio of
164 operational conductance to G_{max} (ζ), boundary layer conductance (G_b), and mesophyll conductance (G_m)
165 (Franks et al., 2014).

166

167

$$G_c = \left(\frac{1}{G_b} + \frac{1}{\zeta \times G_{max}} + \frac{1}{G_m} \right)^{-1} \quad (4)$$

168

169 G_b , ζ , and G_m are all changeable under natural conditions (e.g. Schuepp, 1993; Niinemets et al., 2009;
170 Londoño et al., 2018) and it is highly disputed if these variables can be determined from fossil leaf
171 material at all (e.g. McElwain et al., 2016; Soh et al., 2017). However, we adopt a standardized approach
172 put forward by Franks et al. (2014) to obtain input for these variables. $G_b = 2 \pm 0.1 \text{ mol m}^{-2} \text{ s}^{-1}$, $\zeta = 0.2 \pm$
173 0.02 (Franks et al., 2009; Dow et al., 2014), and G_m is determined using an empirical calibration (Evans
174 and Von Caemmerer, 1996).

175

176

$$G_m = 0.013 \times A_n \quad (5)$$

177



178 G_{max} is determined using predominantly measurable anatomical features of the fossil leaf cuticle (Franks
179 and Beerling, 2009): stomatal density (SD), maximum aperture surface area (a_{max}), pore depth (p_d), and
180 the ratio of diffusivity of CO_2 in air over the molar volume of air (d/v), here taken as $0.000714 \text{ mol m}^{-1} \text{ s}^{-1}$
181 (Marrero and Mason, 1972).

182

183
$$G_{max} = d/v \times SD \times \frac{a_{max}}{p_d + \frac{\pi}{2} \sqrt{a_{max}/\pi}} \quad (6)$$

184

185 In this equation, SD can be measured directly from the leaf, p_d is assumed to be the same as guard cell
186 width (gcw), and a_{max} is determined assuming a circular opening for the aperture, with the measurable
187 pore length (p_l) as the diameter (Franks et al., 2014).

188

189
$$a_{max} = \pi \times \frac{p_l}{4} \quad (7)$$

190

191 Measurements of SD , gcw and p_l used in the Franks et al. (2014) gas-exchange model are presented in
192 Table S1.

193

194 Hence, it is clear that though G_c is largely determined by measurable anatomical parameters, because A_n
195 is a component of calculating G_m , G_c is solved iteratively. However, A_n is also solved iteratively, as it is
196 dependent on C_a and the carbon saturation value (Γ), set at 40 ppm (Franks et al., 2013).

197

198
$$A_n \approx A_0 \times \frac{(C_a - \Gamma) \times (C_{a0} + 2\Gamma)}{(C_a + 2\Gamma) \times (C_{a0} - \Gamma)} \quad (8)$$

199

200 In which A_0 is the photosynthetic rate of a modern model species that can represent the fossil species'
201 photosynthetic rate, and C_{a0} is the atmospheric carbon dioxide level at which A_0 was measured. A_0 for



202 each fossil species was derived from the compilation of photosynthetic rates presented in Reichgelt and
203 D'Andrea (2019). For fossil leaves with known modern relatives, we constrained the possible A_0 range by
204 only including modern relatives within the same family or order, i.e. Lauraceae for *Litsea calicarioides*,
205 *Cryptocarya taieriensis*, *C. maarensis*, cf. *Cryptocarya*, *Beilschmiedia otagoensis* and cf. *Endiandra*,
206 Myrtaceae for cf. Myrtaceae, Liliales for cf. *Ripogonum*, Primulaceae for cf. *Myrsine*, Elaeocarpaceae and
207 Cunoniaceae for cf. Elaeocarpaceae/Cunoniaceae, Meliaceae for cf. Meliaceae, Atherospermataceae for
208 *Laurelia otagoensis*, and Laurales for *Hedycarya pluvisilva*. Then, following the method of constraining
209 A_0 of modern living relatives presented in Reichgelt and D'Andrea (2019), only A_0 values of plants with
210 similar growth forms to the fossil plants, and growing in similar light environments as Foulden Maar were
211 included. A_0 and Ca_0 used in the Franks et al. (2014) model, and associated ecology of fossil leaf types is
212 shown in Table S2.

213

214 The Franks et al. (2014) gas-exchange model thus iteratively solves for C_a , A_n , and G_c . However, only
215 leaves derived from canopy trees are likely to represent these values at light saturation. Moreover, plants
216 in the understory assimilate a mix of atmospheric and respired CO_2 , which has therefore already
217 undergone fractionation processes, making the calculated C_i/C_a problematic. Therefore, we present the
218 results for C_a , A_n , and G_c of leaf types most likely to be derived from canopy trees separately, as they are
219 more likely to not have a systematic skew.

220 $iWUE$ is defined as the ratio between A_n and stomatal conductance to water (Feng, 1999).

221

222
$$iWUE = \frac{A_n}{G_w} \quad (9)$$

223

224 Due to the different rates at which carbon dioxide and water vapor diffuse in air, a transformation of G_c is
225 required to calculate G_w .

226



227
$$G_w = 1.6 \times G_c \quad (10)$$

228

229 Finally, cumulative annual carbon uptake through photosynthesis (A_{tot}) can be calculated in $\text{gC m}^{-2} \text{yr}^{-1}$,
230 by transferring from moles to grams, including a measure for the relative time the leaf is assimilating
231 carbon (ζ), and a measure for the absolute amount of time that the leaf was assimilating carbon.

232

233
$$A_{tot} = (2.6 \times \zeta \times A_n \times GS) \times 12 \quad (11)$$

234

235 In which GS is the length of the growing season, which we can derive from the fossil plant assemblage
236 (Reichgelt et al., 2019), using the method of Spicer et al. (2009). G_w , A_{tot} , and $iWUE$ values for *Litsea*
237 *calicarioides*, *Cryptocarya taiariensis*, *C. maarensis*, cf. Elaeocarpaceae/Cunoniaceae, and cf. Myrtaceae
238 are presented in Table S3. The modern reference A_n and G_w data is derived from Maire et al. (2015),
239 which included coordinates, habit, A_n and G_w data, from which we could then calculate $iWUE$ and A_{tot} .
240

241 **2.4 Comparison to Earth System Sensitivity**

242 Earth System Sensitivity to C_a (ESS) is the amount of temperature increase expected under a doubling of
243 atmospheric CO_2 . This sensitivity is likely not static in Earth's history and is dependent on, among other
244 aspects, continental configuration and ocean circulation patterns (Royer, 2016). ESS is likely to have been
245 between $3\text{--}7^\circ\text{C}$ for the Neogene (Hansen et al., 2013; Royer, 2016), meaning that a doubling of C_a
246 compared to pre-industrial levels would have led to an increase of global average surface temperatures
247 (T_s) of $3\text{--}7^\circ\text{C}$ compared to modern. Using this expected ESS, we calculated the expected C_a using the
248 methodology of Hansen et al. (2013).

249 Compiled deep-sea benthic foraminifera $\delta^{18}\text{O}$ data of the last 30 million years (Zachos et al., 2001)
250 were averaged into 20 kyr time bins. Deep-sea temperatures (T_d) were then calculated using the linear
251 transfer functions of Hansen et al. (2013), which depend on the presence of sea-ice.

252



253
$$T_d = 5 - 8 \times \frac{\delta^{18}O - 1.75}{3} \text{ IF } (\delta^{18}O < 3.25)(12)$$

254
$$T_d = 1 - 4.4 \times \frac{\delta^{18}O - 3.25}{3} \text{ IF } (\delta^{18}O > 3.25)(13)$$

255

256 T_s was then calculated for post-Pliocene using:

257

258
$$T_s = 2 \times T_d + 12.25 \text{ (14)}$$

259 For the Pliocene:

260
$$T_s = 2.5 \times T_d + 12.15 \text{ (15)}$$

261

262 And for pre-Pliocene we assumed that T_s changed linearly with T_d , by a factor of 1.5.

263

264
$$\Delta T_s = 1.5 \times \Delta T_d \text{ (16)}$$

265

266 C_a based on an ESS range of 3–7°C was then calculated using the resulting T_s .

267

268
$$C_a = 310 \times \frac{T_{s[x]} - T_{s[0]}}{2 \times ESS} + 310 \text{ (17)}$$

269

270 In which $T_{s[x]}$ is the calculated average global surface temperature at time x, and $T_{s[0]}$ is the modern day
271 average global surface temperature.

272

273 **3 Results and Discussion**

274 **3.1 Southern Temperate Rainforest Paleocology**

275 Modern day Lauraceae rainforests in New Zealand have a single dominant canopy tree, *Beilschmiedia*

276 *tawa*, and their farthest southern extent is ~42°S (Leathwick, 2001), the farthest southern occurrence of



277 any arborescent Lauraceae species in the world. Rainforests at higher latitudes in New Zealand are
278 usually dominated by Nothofagaceae or Podocarpaceae, and the only modern-day forests at ~50°S are the
279 Magellanic Subpolar Forests in southern South America. Low-growing Podocarpaceae/Nothofagaceae
280 forests, similar to modern forests in southern New Zealand and southern South America, dominated
281 Antarctic vegetation during the early Miocene (Askin and Raine, 2000) and the Foulden Maar rainforest
282 included at least ten Lauraceae species (Bannister et al., 2012), emphasizing the expanded biosphere
283 potential in the early Miocene compared to today (Herold et al., 2010).

284 We identify *L. calicarioides*, *C. maarensis*, *C. taieriensis*, cf. Elaeocarpaceae/Cunoniaceae, and cf.
285 Myrtaceae as the most probable canopy components because they lack 1) the large range of leaf $\delta^{13}\text{C}$
286 values, relatively low overall leaf $\delta^{13}\text{C}$ values (Graham et al., 2014), 2) low cell densities typical of
287 understory components (Kürschner, 1997; Bush et al., 2017) (Fig. 2 a,b), and 3) the undulating or sinuous
288 cell walls typical of understory components (Kürschner, 1997; Bush et al., 2017). The most likely
289 subcanopy or understory taxa were cf. *Ripogonum*, cf. *Myrsine*, “O”, and cf. *Dysoxylum*, because leaf
290 fossils of these types have both low leaf $\delta^{13}\text{C}$ and sinuous or undulating cells (Fig. S1e,f, S2b,d). *H.*
291 *pluvialva*, *L. otagoensis*, cf. *Cryptocarya*, cf. *Endiandra*, *B. otagoensis*, “C”, “H”, “P”, and “Q”, all
292 displayed some variation in these features and occurred in relative low abundance, and are therefore
293 considered of uncertain ecological affinity.

294

295 **3.2 Earliest Miocene CO₂**

296 Gas-exchange modeling (Franks et al., 2014) of canopy leaves throughout the Foulden Maar core
297 indicates that C_a was 445 +618 / -100 ppm, whereas understory elements experienced a higher C_a of 622
298 +3017 / -161 ppm (Fig. 2c), consistent with understory plants assimilating respired CO₂ that has
299 undergone prior fractionation processes, as well as experiencing elevated levels of C_a under the canopy
300 (Graham et al., 2014; Royer et al., 2017). Prior work on the Foulden Maar core established three different
301 phases based on bulk organic $\delta^{13}\text{C}$ (Fig. 1c), fatty acid $\delta^{13}\text{C}$, and fatty acid δD : Phase I (80–105 m depth)
302 with high $\delta^{13}\text{C}$ and low δD , Phase II (55–65 m depth) with low $\delta^{13}\text{C}$ and high δD , and Phase III (0–45 m



303 depth) with high $\delta^{13}\text{C}$ and low δD (Reichgelt et al., 2016). Phase III can be further subdivided into Phase
304 IIIa (30–45 m depth) and IIIb (0–20 m depth), as Phase IIIa exhibits a period of low fatty acid $\delta^{13}\text{C}$ and
305 high δD , which is not expressed in bulk organic $\delta^{13}\text{C}$ (Reichgelt et al., 2016). Gas-exchange modelling on
306 leaves from these phases (Fig. 1c) suggest that during Phase II and IIIa C_a may have been elevated ($C_a =$
307 $529 +1159 / -125$ and $C_a = 538 +769 / -181$ ppm, respectively) compared to Phase I and Phase IIIb ($C_a =$
308 $444 +572 / -95$ and $442 +1219 / -110$ ppm, respectively) (Fig. 3).

309 The advantage of using gas-exchange modeling to reconstruct C_a from multiple species is that the
310 uncertainty is quantified and constrained, greatly reducing the potential for systematic error in the final
311 estimate (Reichgelt and D'Andrea, 2019; Royer et al., 2019). Along with the enhanced accuracy comes a
312 more comprehensive appraisal of uncertainty than is achieved using other proxy approaches (Fig. 4).
313 Proxy error propagation is based on mechanistic variability, grounded in known physical and
314 physiological limits of plant gas-exchange that are understood to be universal (Franks et al., 2014). This
315 differs from empirical proxies, whose uncertainty representation is based on calibration error of modern-
316 day observations without mechanistic constraints. Our canopy C_a estimate ($445 +618 / -100$ ppm, Fig. 2c)
317 is independent of calibration error, based on universal gas-exchange mechanisms, and represents plant
318 vegetative organs of multiple plant species that directly interacted with the available pool of atmospheric
319 carbon dioxide. Previous C_a estimates from the Oligocene/Miocene boundary based on boron isotopes
320 and paleosol carbonates are generally lower than our estimates (Ji et al., 2018; Greenop et al., 2019) (Fig.
321 4b), whereas C_a estimates based on stomatal index and recent alkenone-based C_a estimates are more
322 similar to our results (Kürschner et al., 2008; Super et al., 2018).

323 Reconstructions of globally elevated temperatures of 5–6 °C in the early Miocene (Hansen et al.,
324 2013) with a C_a of ~300 ppm (Ji et al., 2018; Greenop et al., 2019) upsets the expected ESS to C_a during
325 this period (Henrot et al., 2010). Geochemical C_a proxy estimates consistently produce C_a estimates that
326 are too low to satisfy ESS to C_a prior to the Pliocene (Royer, 2016) (Fig. 4a,b). Estimates from the fossil
327 leaf-based stomatal index proxy for C_a (Kürschner et al., 2008) on the other hand do indicate a positive
328 correlation between temperature and C_a in the Neogene (Fig. 4a). At present, there are too few studies that



329 reconstruct C_a using gas-exchange modeling to allow for a full comparison to other C_a proxies; however,
330 our C_a estimates of ~450–550 ppm are in line with the ESS to C_a in the early Miocene (Fig. 4a,b), based
331 on modelling experiments (Herold et al., 2010; Henrot et al., 2010). Moreover, thus far, Neogene C_a
332 estimates reconstructed using gas-exchange methods (Reichgelt et al., 2016; Tesfamichael et al., 2017;
333 Londoño et al., 2018; Moraweck et al., 2019) appear to agree with the suggested ESS to C_a (Fig. 4a,b).
334 Bulk organic and leaf wax $\delta^{13}C$ values reveal a ~4‰ decrease at Foulden Maar over a 10-meter
335 interval at the beginning of Phase II (55–65 m depth), likely representing a time period of <10 kyr (Fox et
336 al., 2016). This shift in isotopic composition suggests a substantial change in the global carbon cycle
337 (Reichgelt et al., 2016). Results presented here show a ~100 ppm C_a increase (from ~450 to 550) from
338 Phase I to Phase II (Fig. 3). The C_a values stay near 550 ppm throughout Phase II and Phase IIIa,
339 representing a 20–40 kyr time period (Fig. 3). Absolute dating of Foulden Maar based on paleomagnetic
340 reversals in the core, annual lamination of lake sediments, and basalt-derived Ar/Ar dates indicates that
341 the deposition of the Foulden Maar sediment coincided with the termination of the earliest Miocene (Mi-
342 1) glaciation of Antarctica (Fox et al., 2015). An increase in C_a from ~450 to ~550 ppm at the termination
343 of Mi-1 is consistent with modeling studies indicating that $C_a > 500$ ppm is necessary to terminate a large-
344 scale Antarctic glaciation (DeConto et al., 2008).

345

346 **3.3 Elevated CO₂ and the early Miocene biosphere**

347 The Foulden Maar Miocene rainforest was primarily evergreen (Lee et al., 2016). The main Miocene
348 canopy trees at Foulden Maar, *Litsea calicarioides*, *Cryptocarya taieriensis*, *C. maarensis*, cf.
349 Elaeocarpaceae/Cunoniaceae and cf. Myrtaceae, had relatively high iWUE (Miocene iWUE first quartile
350 [Q₁] – third quartile [Q₃] = 70–101) compared to modern evergreen trees (evergreen iWUE Q₁–Q₃ = 31–
351 73) (Fig. 5a). Reconstructed iWUE from tropical early Miocene plants (Tesfamichael et al., 2017;
352 Londoño et al., 2018) is slightly higher (Q₁–Q₃ = 80–125) (Fig. 5a). The difference between reconstructed
353 Miocene iWUE and that of modern deciduous trees is greater still (deciduous iWUE Q₁–Q₃ = 27–52),
354 consistent with the expectation that increased C_a favors evergreen trees (Niinemets et al., 2011; Soh et al.,



2019). In contrast to $iWUE$, reconstructed conductance to water (G_w) for Miocene trees is similar to the modern-day range at the same latitude (Fig. 5b), a somewhat surprising result because G_w is expected to be reduced in high C_a climates (Franks and Beerling, 2009). Increased atmospheric evaporative demand in combination with a longer growing season in a warmer climate would facilitate a relatively high hydraulic flux to the atmosphere, despite higher $iWUE$ and similar G_w (Frank et al., 2015). Furthermore, a longer growing season also results in increased total annual carbon flux (A_{tot}) to the biosphere (Fig. 5c). Early Miocene trees at $50^\circ S$ likely assimilated $A_{tot} Q_{1-Q_3} = 265-696 \text{ gC m}^{-2} \text{ yr}^{-1}$, in comparison to $A_{tot} Q_{1-Q_3} = 108-182 \text{ gC m}^{-2} \text{ yr}^{-1}$ in modern evergreen forests, and $A_{tot} Q_{1-Q_3} = 249-410 \text{ gC m}^{-2} \text{ yr}^{-1}$ in modern deciduous forests at the same latitude (Fig. 5c). Tropical trees appear to have slightly higher total annual carbon flux ($A_{tot} Q_{1-Q_3} = 596-1220 \text{ gC m}^{-2} \text{ yr}^{-1}$) than today ($A_{tot} Q_{1-Q_3} = 329-721 \text{ gC m}^{-2} \text{ yr}^{-1}$). Although this estimate cannot take the number of leaves per unit area into account, the results provide strong evidence for enhanced productivity in “greener” worlds.

367

368 4 Conclusions

369 Leaf-level gas-exchange derived C_a estimates suggest that early Miocene atmospheric CO_2 was higher
370 than pre-industrial levels at 450–550 ppm, further solidifying the growing consensus of relatively high
371 early Miocene global temperatures maintained by high atmospheric CO_2 (Kürschner et al., 2009;
372 Tesfamichael et al., 2017; Super et al., 2018; Londoño et al., 2018; Moraweck et al., 2019). A relatively
373 high C_a in the early Miocene also satisfies an Earth System Sensitivity of $3-7^\circ C$ (Hansen et al., 2013;
374 Royer, 2016). A potential shift in atmospheric CO_2 from 450 to 550, and back to 450, is recorded in the
375 100 kyr of sedimentation and leaf deposition at Foulden Maar. A disruption of the regional carbon and
376 hydrological cycle was also recorded in leaf-wax $\delta^{13}C$ and δD (Reichgelt et al., 2016), and may be linked
377 to the Antarctic deglaciation at the termination of the Mi-1 (DeConto et al., 2008; Fox et al., 2015;
378 Liebrand et al., 2017).

379 The first record is provided of increased Miocene leaf-level intrinsic water-use efficiency in both
380 temperate New Zealand and the tropics, and we provide evidence for increased leaf-level productivity in



381 temperate New Zealand. Enhanced productivity and water-use efficiency on other landmasses in
382 temperate latitudes during the early Miocene, such as North America, Australia, and Asia, would have
383 had a major impact on the global carbon and water cycles. Our gas-exchange results from New Zealand,
384 supplemented with results from Ethiopia (Tesfamichael et al., 2017) and Panama (Londoño et al., 2018)
385 provide empirical evidence for high water-use efficiency in the globally warmer world of the early
386 Miocene, associated with elevated C_a . Tropical trees with high water-use efficiency compared to modern,
387 would have likely facilitated forest survival in climates where currently tropical savannas and grasslands
388 exist. An overall higher water-use efficiency in the early Miocene tropics is corroborated by the spread of
389 C_4 grasslands in the late Miocene, when reduced CO_2 levels started favoring the more efficient C_4
390 photosynthetic pathway (Strömberg, 2011; Polissar et al., 2016).

391 Emission scenarios suggest that atmospheric CO_2 will reach our reconstructed early Miocene values of
392 450 ppm by 2030–2040 CE. While the global temperature response may lag the C_a increase, and forest
393 habitat expansion is hampered by the slow dispersal and growth rate of climax forest trees and
394 anthropogenic influence (e.g., forest fragmentation and fire), early Miocene water-use efficiency and
395 productivity estimates provide insight into the near future-biosphere potential, as well as into selective
396 pressures that influence the types of plants that may proliferate under future elevated C_a .

397

398 **Acknowledgments.** We thank the Gibson family for kindly allowing us access to the site. Funding for
399 this research was provided by a Royal Society of New Zealand Marsden grant (UOO1115) to DEL, an
400 NSF grant (EAR13-49659) to WJD, a Vetlesen Foundation Climate Center grant to TR and WJD, and the
401 Lamont-Doherty Earth Observatory Summer Internship Program for Undergraduates awarded to ACVM.
402 Wei Huang, Andy Juhl and Nicole DeRoberts are acknowledged for technical support.

403

404 **Author contributions.** TR and WJD conceived of the idea and performed data analyses. BRSF and DEL
405 collected sediment core, BRSF and TR sampled the sediment core, JGC and JMB identified fossil leaf



406 taxa. ACVM and TR gathered data from fossil leaves. TR and WJD wrote the paper and all authors
407 contributed to the final manuscript.

408

409 **Competing interests.** The authors declare no competing interests.

410

411 **References**

- 412 Askin, R. A. and Raine, J. I.: Oligocene and early Miocene terrestrial palynology of the Cape Roberts
413 drillhole CRP-2/2A, Victoria Land Basin, Antarctica, *Terra Antarctica*, 7, 493–501, 2000.
- 414 Bannister, J. M., Conran, J. G., and Lee, D. E.: Lauraceae from rainforest surrounding an early Miocene
415 maar lake, Otago, southern New Zealand, *Review of Palaeobotany and Palynology*, 178, 13–34, 2012.
- 416 Bar-On, Y. M., Philips, R., and Milo, R.: The biomass distribution on Earth, *PNAS*, 115, 6506–6511,
417 2018.
- 418 Beer, C., Reichstein, M., Tomelleri, E., Ciais, P., Jung, M., Carvalhais, N., Rödenbeck, C., Arain, M. A.,
419 Baldocchi, D., Bonan, G. B., Bondeau, A., Cescatti, A., Lasslop, G., Lindroth, A., Lomas, M.,
420 Luyssaert, S., Margolis, H., Oleson, K. W., Rouspard, O., Veenendaal, E., Viovy, N., Williams, C. J.,
421 Woodward, F. I., and Papale, D.: Terrestrial gross carbon dioxide uptake: Global distribution and
422 covariation with climate, *Science*, 329, 834–838, 2010.
- 423 Bolton, C. T., Hernández-Sánchez, M. T., Fuertes, M.-Á., González-Lemos, S., Abrevaya, L., Mendez-
424 Vicente, A., Flores, J.-A., Probert, I., Giosan, L., Johnson, J., and Stoll, H. M.: Decrease in
425 coccolithophore calcification and CO₂ since the middle Miocene, *Nature Communications*, 7, 1–13,
426 2016.
- 427 Boyden, J. A., Müller, R. D., Gurnis, M., Torsvik, T. H., Clark, J. A., Turner, M., Ivey-Law, H., Watson,
428 R. J., and Cannon, J. S.: Next-generation plate-tectonic reconstructions using GPlates. In:
429 *Geoinformatics: Cyberinfrastructures for the Solid Earth Sciences*, Keller, G. R. and Baru, C. (Eds.),
430 Cambridge University Press, 2011.
- 431 Bush, R. T., Wallace, J., Currano, E. D., Jacobs, B. F., McInerney, F. A., Dunn, R. E., and Tabor, N. J.:
432 Cell anatomy and leaf $\delta^{13}\text{C}$ as proxies for shading and canopy structure in a Miocene forest from
433 Ethiopia, *Palaeogeography, Palaeoclimatology, Palaeoecology*, 485, 593–604, 2017.
- 434 Cernusak, L. A.: Gas exchange and water-use efficiency in plant canopies, *Plant Biology*, 22, 52–67,
435 2020.
- 436 Conran, J. G., Bannister, J. M., and Lee, D. E.: Fruits and leaves with cuticle of *Laurelia otagoensis* sp.
437 nov. (Atherospermataceae) from the early Miocene of Otago (New Zealand), *Alcheringa*, 37, 1–14,
438 2013.
- 439 Conran, J. G., Lee, W. G., Lee, D. E., Bannister, J. M., and Kaulfuss, U.: Reproductive niche
440 conservatism in the isolated New Zealand flora over 23 million years, *Biology Letters*, 10, 20140647,
441 2014.
- 442 Conran, J. G., Bannister, J. M., Mildenhall, D. C., and Lee, D. E.: *Hedycarya* macrofossils and associated
443 *Planarpollenites* pollen from the early Miocene of New Zealand, *American Journal of Botany*, 103,
444 938–956, 2016.



- 445 DeConto, R. M., Pollard, D., Wilson, P. A., Pälike, H., Lear, C. H., and Pagani, M.: Thresholds for
446 Cenozoic bipolar glaciation, *Nature*, 455, 652–656, 2008.
- 447 Dow, G. J., Bergmann, D. C., and Berry, J. A.: An integrated model of stomatal development and leaf
448 physiology, *New Phytologist*, 201, 1218–1226, 2014.
- 449 Drake, B. G., González-Meler, M. A., and Long, S. P.: More efficient plants: A consequence of rising
450 atmospheric CO₂?, *Annual Review of Plant Physiology and Plant Molecular Biology*, 48, 606–639,
451 1997.
- 452 Evans, J. R. and Von Caemmerer, S.: Carbon dioxide diffusion inside leaves, *Plant Physiology*, 110, 339–
453 346, 1996.
- 454 Farquhar, G. D., von Caemmerer, S., and Berry, J. A.: A biochemical model of photosynthetic CO₂
455 assimilation in leaves of C₃ species, *Planta*, 149, 78–90, 1980.
- 456 Farquhar, G. D., O'Leary, M. H., and Berry, J. A.: On the relationship between carbon isotope
457 discrimination and the intercellular carbon dioxide concentration in leaves, *Australian Journal of Plant*
458 *Physiology*, 9, 121–137, 1982.
- 459 Farquhar, G. D. and Richards, R. A.: Isotopic composition of plant carbon correlates with water-use
460 efficiency of wheat genotypes, *Australian Journal of Plant Physiology*, 11, 539–552, 1984.
- 461 Farquhar, G. D., Ehleringer, J. R., and Hubick, K. T.: Carbon isotope discrimination and photosynthesis,
462 *Annual Review of Plant Physiology and Plant Molecular Biology*, 40, 503–537, 1989.
- 463 Foster, G. L., Royer, D. L., and Lunt, D. J.: Future climate forcing potentially without precedent in the last
464 420 million years, *Nature Communications*, 8, 14845, 2017.
- 465 Feng, X.: Trends in intrinsic water-use efficiency of natural trees for the past 100–200 years: a response
466 to atmospheric CO₂ concentration, *Geochimica et Cosmochimica Acta*, 63, 1891–1903, 1999.
- 467 Fox, B. R. S., Wartho, J.-A., Wilson, G. S., Lee, D. E., Nelson, F. E., and Kaulfuss, U.: Long-term
468 evolution of an Oligocene/Miocene maar lake from Otago, New Zealand, *Geochemistry, Geophysics,*
469 *Geosystems*, 16, 59–76, 2015.
- 470 Fox, B. R. S., Wilson, G. S., and Lee, D. E.: A unique annually laminated maar lake sediment record
471 shows orbital control of Southern Hemisphere midlatitude climate across the Oligocene-Miocene
472 boundary, *Geological Society of America Bulletin*, 128, 609–626, 2016.
- 473 Frank, D. C., Poulter, B., Saurer, M., Esper, J., Huntingford, C., Helle, G., Treydte, K., Zimmermann, N.
474 E., Schleser, G. H., Ahlström, A., Ciais, P., Friedlingstein, P., Levis, S., Lomas, M., Sitch, S., Viovy,
475 N., Andreu-Hayles, L., Bednarz, Z., Berninger, F., Boettger, T., D'Alessandro, H., Kalela-Brundin, M.,
476 Krapiec, M., Leuenberger, M., Loader, N. J., Marah, H., Masson-Delmotte, V., Pazdur, A., Pawelczyk,
477 S., Pierre, M., Planells, O., Pukiene, R., Reynolds-Henne, C. E., Rinne, K. T., Saracino, A., Sonninen,
478 E., Stievenard, M., Switsur, V. R., Szczepanek, E., Szychowska-Krapiec, L., Todaro, L., Waterhouse,
479 J. S., and Weigl, M.: Water-use efficiency and transpiration across European forests during the
480 Anthropocene, *Nature Climate Change*, 5, 579–583, 2015.
- 481 Franks, P. J. and Beerling, D. J.: Maximum leaf conductance driven by CO₂ effects on stomatal size and
482 density over geologic time, *PNAS*, 106, 10343–10347, 2009.
- 483 Franks, P. J., Drake, P. L., and Beerling, D. J.: Plasticity in maximum stomatal conductance constrained
484 by negative correlation between stomatal size and density: an analysis using *Eucalyptus globulus*,
485 *Plant, Cell and Environment*, 32, 1737–1748, 2009.
- 486 Franks, P. J., Adams, M. A., Amthor, J. S., Barbour, M. M., Berry, J. A., Ellsworth, D. S., Farquhar, G.
487 D., Ghannoum, O., Lloyd, J., McDowell, N. G., Norby, R. J., Tissue, D. T., and von Caemmerer, S.:



- 488 Sensitivity of plants to changing atmospheric CO₂ concentration: from the geological past to the next
489 century, *New Phytologist*, 197, 1077–1094, 2013.
- 490 Franks, P. J., Royer, D. L., Beerling, D. J., van de Water, P. K., Cantrill, D. J., Barbour, M. M., and
491 Berry, J. A.: New constraints on atmospheric CO₂ concentration for the Phanerozoic, *Geophysical*
492 *Research Letters*, 41, 4685–4694, 2014.
- 493 Greenop, R., Sossian, S. M., Henehan, M. J., Wilson, P. A., Lear, C. H., and Foster, G. L.: Orbital
494 forcing, ice volume, and CO₂ across the Oligocene–Miocene transition, *Paleoceanography and*
495 *Paleoclimatology*, 34, 316–628, 2019.
- 496 Hansen, J., Sato, M., Russell, G., and Kharecha, P.: Climate sensitivity, sea level and atmospheric carbon
497 dioxide, *Philosophical Transactions of the Royal Society A*, 371, 20120294, 2013.
- 498 Graham, H. V., Patzkowsky, M. E., Wing, S. L., Parker, G. G., Fogel, M. L., and Freeman, K. H.:
499 Isotopic characteristics of canopies in simulated leaf assemblages, *Geochimica et Cosmochimica Acta*,
500 144, 82–95, 2014.
- 501 Henrot, A.-J., François, L., Favre, E., Butzin, M., Ouberdous, M., and Munhoven, G.: Effects of CO₂,
502 continental distribution, topography and vegetation changes on the climate at the Middle Miocene: a
503 model study, *Climate of the Past*, 6, 675–694, 2010.
- 504 Herold, N., Müller, R. D., and Seton, M.: Comparing early to middle Miocene terrestrial climate
505 simulations with geological data, *Geosphere*, 6, 952–961, 2010.
- 506 Ji, S., Nie, J., Lechler, A., Huntington, K. W., Heitmann, E. O., and Breecker, D. O.: A symmetrical CO₂
507 peak and asymmetrical climate change during the middle Miocene, *Earth and Planetary Science*
508 *Letters*, 499, 134–144, 2018.
- 509 Kaulfuss, U.: Crater stratigraphy and the post-eruptive evolution of Foulden Maar, southern New
510 Zealand, *New Zealand Journal of Geology and Geophysics*, 60, 410–432, 2017.
- 511 Kaulfuss, U., Lee, D. E., Barratt, B. I. P., Leschen, R. A. B., Larivière, M.-C., Dlussky, G. M.,
512 Henderson, I. M., and Harris, A. C.: A diverse fossil terrestrial arthropod fauna from New Zealand:
513 evidence from the early Miocene Foulden Maar fossil lagerstätte, *Lethaia*, 48, 299–308, 2015.
- 514 Kürschner, W. M.: The anatomical diversity of recent and fossil leaves of the durmast oak (*Quercus*
515 *petraea* Lieblein/*Q. pseudocastanaea* Goeppert) — implications for their use as biosensors of
516 palaeoatmospheric CO₂ levels, *Review of Palaeobotany and Palynology*, 96, 1–30, 1997.
- 517 Kürschner, W. M., Kvaček, Z., and Dilcher, D. L.: The impact of Miocene atmospheric carbon dioxide
518 fluctuations on climate and the evolution of terrestrial ecosystems, *PNAS*, 105, 449–453, 2008.
- 519 Kürschner, W. M. and Kvaček, Z.: Oligocene–Miocene CO₂ fluctuations, climatic and palaeofloristic
520 trends inferred from fossil plant assemblages in central Europe, *Bulletin of Geosciences*, 84, 189–202,
521 2009.
- 522 Leathwick, J. R.: New Zealand's potential forest pattern as predicted from current species–environment
523 relationships, *New Zealand Journal of Botany*, 39, 447–464, 2001.
- 524 Lee, D. E., Lindqvist, J. K., Beu, A. G., Robinson, J. H., Ayress, M. A., Morgans, H. E. G., and Stein, J.
525 K.: Geological setting and diverse fauna of a Late Oligocene rocky shore ecosystem, Cosy Dell,
526 Southland, *New Zealand Journal of Geology and Geophysics*, 57, 195–208, 2014.
- 527 Lee, D. E., Kaulfuss, U., Conran, J. G., Bannister, J. M., and Lindqvist, J. K.: Biodiversity and
528 palaeoecology of Foulden Maar: an early Miocene *Konservat-Lagerstätte* deposit in southern New
529 Zealand, *Alcheringa*, 40, 525–541, 2016.
- 530 Liebrand, D., de Bakker, A. T. M., Beddow, H. M., Wilson, P. A., Bohaty, S. M., Ruessink, G., Pälke,
531 H., Batenburg, S. J., Hilgen, F. J., Hodell, D. A., Huck, C. E., Kroon, D., Raffi, I., Saes, M. J. M., van



- 532 Dijk, A. E., and Lourens, L. J.: Evolution of the early Antarctic ice ages, *PNAS*, 114, 3867–3872,
533 2017.
- 534 Lindqvist, J. K. and Lee, D. E.: High-frequency paleoclimate signals from Foulden Maar, Waipiata
535 Volcanic Field, southern New Zealand: An Early Miocene varved lacustrine diatomite deposit,
536 *Sedimentary Geology*, 222, 98–110, 2009.
- 537 Londoño, L., Royer, D. L., Jaramillo, C. A., Escobar, J., Foster, D. A., Cárdenas-Rozo, A. L., and Wood,
538 A.: Early Miocene CO₂ estimates from a Neotropical fossil leaf assemblage exceed 400 ppm,
539 *American Journal of Botany*, 105, 1929–1937, 2018.
- 540 Maire, V., Wright, I. J., Prentice, I. C., Batjes, N. H., Bhaskar, R., van Bodegom, P. M., Cornwell, W. K.,
541 Ellsworth, D. S., Niinemets, Ü., Ordonez, A., Reich, P. B., and Santiago, L. S.: Global effects of soil
542 and climate on leaf photosynthetic traits and rates, *Global Ecology and Biogeography*, 24, 706–717,
543 2015.
- 544 Marrero, T. R. and Mason, E. A.: Gaseous diffusion coefficients, *Journal of Physical and Chemical*
545 *Reference Data*, 1, 3–118, 1972.
- 546 McElwain, J. C., Montañez, I. P., White, J. D., Wilson, J. P., and Yiotis, C.: Was atmospheric CO₂ capped
547 at 1000 ppm over the past 300 million years?, *Palaeogeography, Palaeoclimatology, Palaeoecology*,
548 441, 653–658, 2016.
- 549 Moraweck, K., Grein, M., Konrad, W., Kvaček, J., Kovar-Eder, J., Neinhuis, C., Traiser, C., and
550 Kunzmann, L.: Leaf traits of long-ranging Paleogene species and their relationship with depositional
551 facies, climate and atmospheric CO₂ level, *Palaeontographica Abteilung B*, 298, 93–172, 2019.
- 552 Németh, K. and White, J. D. L.: Reconstructing eruption processes of a Miocene monogenetic volcanic
553 field from vent remnants: Waipiata Volcanic Field, South Island, New Zealand, *Journal of*
554 *Volcanology and Geothermal Research*, 124, 1–21, 2003.
- 555 Niinemets, Ü., Díaz-Espejo, A., Flexas, J., Galmés, J., and Warren, C. R.: Role of mesophyll diffusion
556 conductance in constraining potential photosynthetic productivity in the field, *Journal of Experimental*
557 *Botany*, 60, 2249–2270, 2009.
- 558 Niinemets, Ü., Flexas, J., and Peñuelas, J.: Evergreens favored by higher responsiveness to increased
559 CO₂, *TRENDS in Ecology and Evolution*, 26, 136–142, 2011.
- 560 Polissar, P. J., Rose, C., Uno, K. T., Phelps, S. R., and DeMenocal, P.: Synchronous rise of African C₄
561 ecosystems 10 million years ago in the absence of aridification, *Nature Geoscience*, 12, 657–660,
562 2016.
- 563 Reichgelt, T., Kennedy, E. M., Mildenhall, D. C., Conran, J. G., Greenwood, D. R., and Lee, D. E.:
564 Quantitative palaeoclimate estimates for Early Miocene southern New Zealand: Evidence from
565 Foulden Maar, *Palaeogeography, Palaeoclimatology, Palaeoecology*, 378, 36–44, 2013.
- 566 Reichgelt, T., D'Andrea, W. J., and Fox, B. R. S.: Abrupt plant physiological changes in southern New
567 Zealand at the termination of the Mi-1 event reflect shifts in hydroclimate and *p*CO₂, *Earth and*
568 *Planetary Science Letters*, 455, 115–124, 2016.
- 569 Reichgelt, T. and D'Andrea, W. J.: Plant carbon assimilation rates in atmospheric CO₂ reconstructions,
570 *New Phytologist*, 223, 1844–1855, 2019.
- 571 Reichgelt, T., Kennedy, E. M., Conran, J. G., Lee, W. G., and Lee, D. E.: The presence of moisture
572 deficits in Miocene New Zealand, *Global and Planetary Change*, 172, 268–277, 2019.
- 573 Roeske, C. A. and O'Leary, M. H.: Carbon isotope effects on the enzyme-catalyzed carboxylation of
574 ribulose biphosphate, *Biochemistry*, 23, 6275–6284, 1984.



- 575 Royer, D. L.: Climate sensitivity in the geologic past, *Annual Review of Earth and Planetary Sciences*,
576 44, 277–293, 2016.
- 577 Royer, D. L., Moynihan, K. M., McKee, M. L., Londoño, L., and Franks, P. J.: Sensitivity of a leaf gas-
578 exchange model for estimating paleoatmospheric CO₂ concentration, *Climate of the Past*, 15, 795–809,
579 2019.
- 580 Rubel, F. and Kotteck, M.: Observed and projected climate shifts 1901–2100 depicted by world maps of
581 the Köppen-Geiger climate classification, *Meteorologische Zeitschrift*, 19, 135–141, 2010.
- 582 Šantrůček, J., Vráblová, M., Šimková, M., Hronková, M., Drtinová, M., Květoň, J., Vrábl, D., Kubásek,
583 J., Macková, J., Wiesnerová, D., Neuwithová, J., and Schreiber, L.: Stomatal and pavement cell
584 density linked to leaf internal CO₂ concentration, *Annals of Botany*, 114, 191–202, 2014.
- 585 Schneider, C. A., Rasband, W. S., and Eliceiri, K. W.: NIH Image to ImageJ: 25 years of image analysis,
586 *Nature Methods*, 9, 671–675, 2012.
- 587 Schuepp, P. H.: Transley Review No. 59 Leaf boundary layers, *New Phytologist*, 125, 477–507, 1993.
- 588 Soh, W. K., Wright, I. J., Bacon, K. L., Lenz, T. I., Steinhorsdottir, M., Parnell, A. C., and McElwain, J.
589 C.: Palaeo leaf economics reveal a shift in ecosystem function associated with the end-Triassic mass
590 extinction event, *Nature Plants*, 3, 8, 2017.
- 591 Soh, W. K., Yiotis, C., Murray, M., Parnell, A. C., Wright, I. J., Spicer, R. A., Lawson, T., Caballero, R.,
592 and McElwain, J. C.: Rising CO₂ drives divergence in water use efficiency of evergreen and deciduous
593 plants, *Science Advances*, 5, eaax7906, 2019.
- 594 Spicer, R. A., Valdes, P. J., Spicer, T. E. V., Craggs, H. J., Srivastava, G., Mehrotra, R. C., and Yang, J.:
595 New developments in CLAMP: Calibration using global gridded meteorological data,
596 *Palaeogeography, Palaeoclimatology, Palaeoecology*, 283, 91–98, 2009.
- 597 Steinhorsdottir, M., Vajda, V., and Pole, M. S.: Significant transient *p*CO₂ perturbation at the New
598 Zealand Oligocene–Miocene transition recorded by fossil plant stomata, *Palaeogeography,
599 Palaeoclimatology, Palaeoecology*, 515, 152–161, 2019.
- 600 Strömberg, C. A. E.: Evolution of grasses and grassland ecosystems, *Annual Review of Earth and
601 Planetary Sciences*, 39, 517–544, 2011.
- 602 Super, J. R., Thomas, E., Pagani, M., Huber, M., O'Brien, C., and Hull, P. M.: North Atlantic temperature
603 and *p*CO₂ coupling in the early-middle Miocene, *Geology*, 46, 519–522, 2018.
- 604 Tesfamichael, T., Jacobs, B. F., Tabor, N. J., Michel, L., Currano, E. D., Feseha, M., Barclay, R. S.,
605 Kappelman, J., and Schmitz, M.: Settling the issue of "decoupling" between atmospheric carbon
606 dioxide and global temperature: [CO₂]_{atm} reconstructions across the warming Paleogene–Neogene
607 divide, *Geology*, 45, 999–1002, 2017.
- 608 Tipple, B. J., Meyers, S. R., and Pagani, M.: Carbon isotope of Cenozoic CO₂: A comparative evaluation
609 of available geochemical proxies, *Paleoceanography*, 25, PA3202, 2010.
- 610 Witkowski, C. R., Agostini, S., Harvey, B. P., van der Meer, M. T. J., Sinnighe Damsté, J. S., and
611 Schouten, S.: Validation of carbon isotope fractionation in algal lipids as a *p*CO₂ proxy using a natural
612 CO₂ seep (Shikine Island, Japan), *Biogeosciences*, 16, 4451–4461, 2019.
- 613 Zachos, J. C., Pagani, M., Sloan, L., Thomas, E., and Billups, K.: Trends, rhythms, and aberrations in
614 global climate 65 Ma to present, *Science*, 292, 686–693, 2001.
- 615 Zhou, S., Yu, B., Shwalm, C. R., Ciais, P., Zhang, Y., Fisher, J. B., Michalak, A. M., Wang, W., Poulter,
616 B., Huntzinger, D. N., Niu, S., Mao, J., Jain, A., Ricciuto, D. M., Shi, X., Ito, A., Wei, Y., Huang, Y.,
617 and Wang, G.: Response of water use efficiency to global environmental change based on output from
618 terrestrial biosphere models, *Global Biogeochemical Cycles*, 31, 1639–1655, 2017.

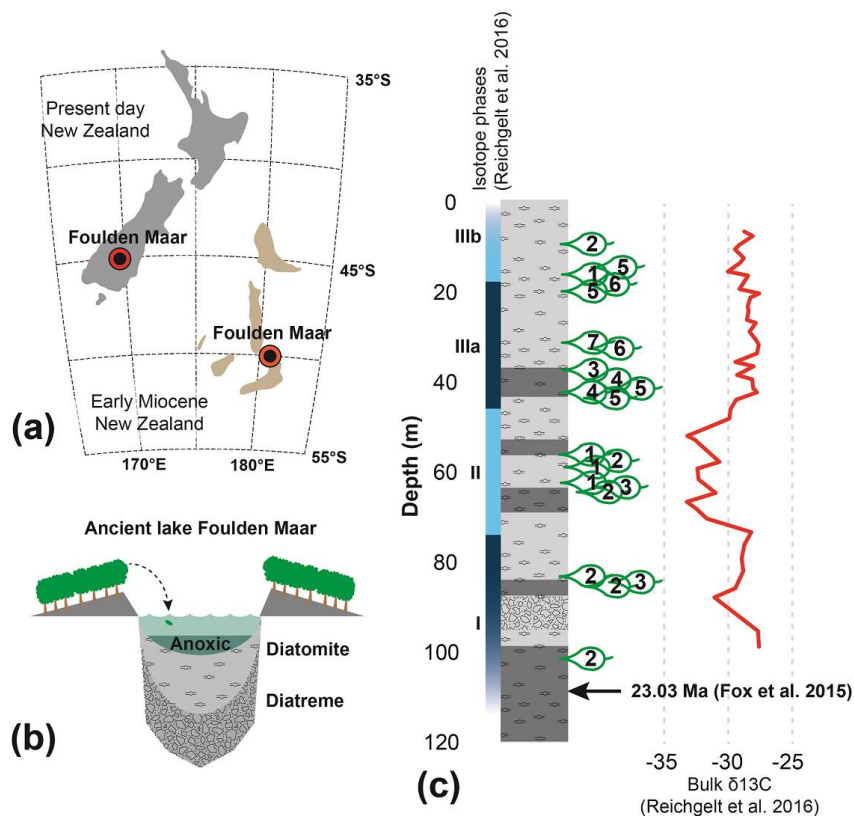


619 Zhu, Z., Piao, S., Myneni, R. B., Zeng, Z., Canadell, J. G., Ciais, P., Sitch, S., Friedlingstein, P., Armeth,
620 A., Cao, C., Cheng, L., Kato, E., Koven, C., Li, Y., Lian, X., Liu, Y., Liu, R., Mao, J., Pan, Y., Peng,
621 S., Peñuelas, J., Poulter, B., Pugh, T. A. M., Stocker, B. D., Viovy, N., Wang, X., Wang, Y., Xiao, Z.,
622 Yang, H., Zaehle, S., and Zeng, N.: Greening of the Earth and its drivers, *Nature Climate Change*, 6,
623 791–795, 2016.
624
625



626 Figure and Figure legends

627



628

629 **Figure 1.** Foulden Maar site information. (a) Location of the Foulden Maar deposit and paleogeographic

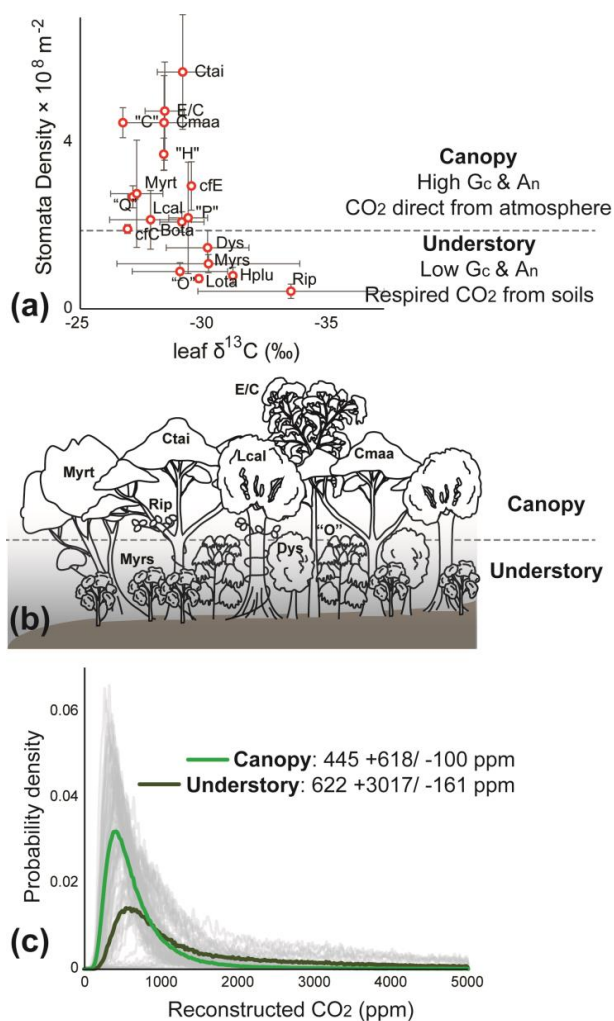
630 reconstruction of early Miocene New Zealand (Boyden et al., 2011; Lee et al., 2014). (b) Schematic

631 reconstruction of the Foulden Maar depositional environment. (c) Stratigraphic column of the Foulden

632 Maar core (Fox et al., 2015), with sample locations and bulk organic $\delta^{13}C$ (Reichgelt et al., 2016).

633

634 Fig. 2

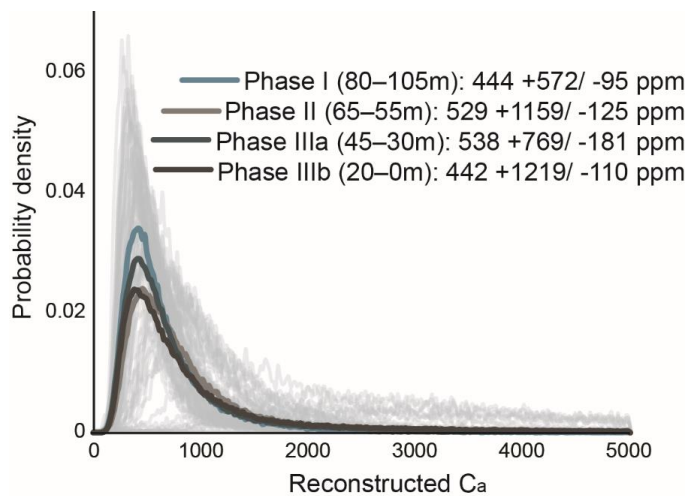


635

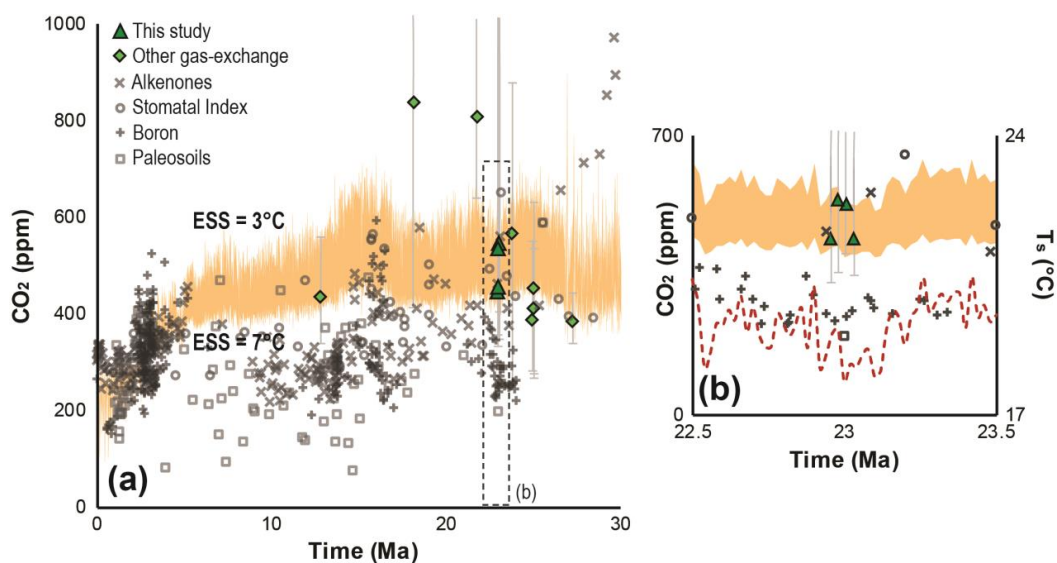
636 **Figure 2. Foulden Maar paleoecology and atmospheric CO_2 reconstructions.** (a) $\delta^{13}\text{C}$ values and
 637 stomatal density from the fossil leaves of Foulden Maar provide constraints to distinguish canopy leaf
 638 types from understory, because understory leaves tend to have a high range of $\delta^{13}\text{C}$ and low cell density
 639 (Graham et al., 2014; Bush et al., 2017). (b) Paleoecological reconstruction of the dense rainforest at
 640 Foulden Maar with a canopy comprising *Litsea calicarioides* (Lcal), *Cryptocarya taieriensis* (Ctai), *C.*
 641 *maarensis* (Cmaa), cf. Elaeocarpaceae/Cunoniaceae (E/C), and cf. Myrtaceae (Myrt), and an understory
 642 comprising cf. *Myrsine* (Myrs), cf. *Ripogonum* (Rip), cf. *Dysoxylum* (Dys), and leaf type "O". *Hedycarya*



643 *pluvisilva* (Hplu), *Laurelia otagoensis* (Lota), *Beilschmiedia otagoensis* (Bota), cf. *Cryptocarya* (cfC), cf.
644 *Endiandra* (cfE), and leaf types “C”, “H”, “P”, and “Q” could not be ecologically placed with certainty.
645 (c) Probability density distributions of C_a reconstructions from canopy (thick light green line) and
646 understory components (thick dark green line) using a gas-exchange model (Franks et al., 2014). Grey
647 curves represent 1000 Monte Carlo reconstructions on a single fossil leaf.
648



649
650 **Figure 3.** Probability density distributions of C_a reconstructions using a gas-exchange model (Franks et
651 al., 2014), divided by bulk carbon isotope phases (Fig. 1c).
652
653 Fig. 4

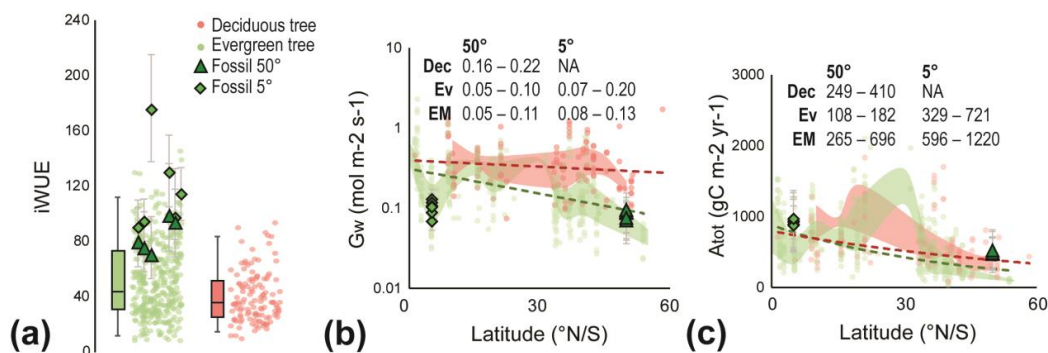


654

655 **Figure 4. Neogene Earth System Sensitivity (ESS) and C_a reconstructions.** Calculated C_a levels for an
656 ESS range of 3–7 °C (orange shaded area) for the last 30 Ma (a), and for the interval between 22.5–23.5
657 Ma (b), the red dashed line in (b) indicates the global average surface temperature (T_s) in the earliest
658 Miocene (Hansen et al., 2013). The ESS envelope was determined using deep-sea δ¹⁸O of benthic
659 foraminifera (Zachos et al., 2001) and the transform function approach from Hansen et al. (2013)
660 (Supplementary Information). Proxy-based Neogene C_a reconstructions are derived from a previously
661 published compilation (Foster et al., 2017) and are supplemented with more recently published data (Ji
662 et al., 2019; Londoño et al., 2018; Super et al., 2018; Greenop et al., 2019; Moraweck et al., 2019,
663 Steinhorsdottir et al., 2019). Error bars on gas-exchange based proxy estimates represent ±1σ.

664

665 Fig. 5



666

667 **Figure 5. Early Miocene leaf-level physiological parameters of canopy trees.** (a) Intrinsic water-use
668 efficiency (iWUE) of evergreen (green circles) and deciduous trees (red circles) based on modern leaf-
669 level measurements (Maire et al., 2015), and fossil reconstructions (green triangles and diamonds). Error
670 bars on fossil-derived data indicate $\pm 1\sigma$, box-and-whisker plots indicate median, first and third quartile
671 (Q1 and Q3), and 95% confidence interval of modern leaves of canopy trees. Individual datapoints are
672 randomized on the x-axis for a clearer depiction of the distribution. (b) Conductance to water (G_w) from
673 modern evergreen (Ev) and deciduous (Dec) trees (Maire et al., 2015) and fossils (EM) from different
674 latitudes. The shaded red and green areas indicate the Q1–Q3 range of modern evergreen and deciduous
675 trees, respectively, and the dashed lines indicate the overall linear trend with latitude. Text in panel is the
676 Q1–Q3 range for each group, grouped in 5° latitude bins. (c) Total annual carbon flux per unit leaf area
677 (A_{tot}) from modern evergreen (Ev) and deciduous (Dec) trees (Maire et al., 2015) and fossils (EM) from
678 different latitudes. The shaded red and green areas indicate the Q1–Q3 range of modern evergreen and
679 deciduous trees, respectively, and the dashed lines indicate the overall exponential trend with latitude.
680 Text in panel is the Q1–Q3 range for each group, grouped in 5° latitude bins.

681

682 **Data availability.** All raw measurement data on fossil leaves generated for this paper is available in the
683 online supplementary information. Raw measurements on fossil leaves from Ethiopia (Tesfamichael et
684 al., 2017) and Panama (Londoño et al., 2018), $\delta^{18}\text{O}$ measurements (Zachos et al., 2001), and iWUE, G_w



685 and A_n measurements on modern plants (Maire et al., 2015) are available through the cited original

686 works.

687